General relationship between the band-gap energy and iodine-oxygen bond distance in metal iodates

Akun Liang,[1] Robin Turnbull,[1] Placida Rodríguez-Hernandez,[2] Alfonso Muñoz,[2] M. Jasmin,[3] Lan-Ting Shi,[4] and Daniel Errandonea[1,*]

[1]*Departamento de Física Aplicada-ICMUV-MALTA Consolider Team, Universitat de València, c/Dr. Moliner 50, Burjassot (Valencia) 46100, Spain*

[2]*Departamento de Física and Instituto de Materiales y Nanotecnología, MALTA Consolider Team, Universidad de La Laguna, La Laguna 38206, Tenerife, Spain*

[3]*TKM College of Arts and Science, Kollam, Kerala 691005, India*

[4]*College of Physics, Sichuan University, Chengdu 610065, China*

(Received 10 March 2022; revised 9 April 2022; accepted 13 April 2022; published 28 April 2022)

A wide band gap is a fundamental requirement for an ideal nonlinear optical material. A two-step investigation has been implemented to determine the relationship between the band-gap energy and the iodine-oxygen bond distance in optically nonlinear metal iodate materials. Firstly, we utilized high-pressure conditions on Mg and Zn iodates to correlate the pressure-induced changes in band-gap energy with changes in the iodine-oxygen bond distances. On both cases, the band-gap energy shows a nonlinear decrease under compression. The nonlinear behavior is a consequence of the interplay between the pressure-induced increase of the first-nearest neighbor iodine-oxygen bonds, which favors a narrowing of the band gap, and the decrease of the second-nearest neighbor iodine-oxygen bonds, which favors an opening of the band gap. The inverse correlation between the band-gap energy and the iodine-oxygen bond distance is confirmed in the second part of the investigation by collating and comparing the band-gap energies and corresponding average iodine-oxygen bond distances of the metal iodates reported in the literature. In the comparison, only nontransition and closed-shelled transition metals were included, without regard for their chemical formula, crystal structure, or stoichiometry.

DOI: 10.1103/PhysRevMaterials.6.044603

I. INTRODUCTION

The search for the next-generation nonlinear optical (NLO) materials has driven the synthesis and characterization of numerous new metal iodates, wherein the metal element covers alkali metals [1,2], alkaline-earth metals [3,4], transition and post-transition metals [4,5] as well as lanthanide elements [6]. In these different compounds, the iodate molecules exhibit different configurational geometries, such as isolated $[IO_3]^-$ trigonal pyramids [7,8], $[I_2O_5]$ [3], $[I_3O_8]^-$ [5,9], and $[I_4O_{11}]^{2-}$ dimeric chains [3]. An ideal NLO crystal should have a high laser damage threshold (LDT), an excellent thermal stability, a wide transparency window which means a wide band-gap energy, and a large second-harmonic generation response (SHG) [10]. Notably, control of the band gap in the designed NLO materials is essential because the band gap directly determines the transparency. In addition, a large band gap may achieve a high LDT [11], and, typically, the band gap has a significant effect on the SHG response [12]. Therefore, it is important to understand which general factors affect the band-gap energy in the various metal iodates which have different chemical formula. Here, we use pressure to investigate the band-gap change of metal iodates because pressure is an efficient tool to manipulate the interaction between atoms and, therefore, to engineer the band gap in semiconductor materials [13,14]. In a previous work we found that iron iodate, $Fe(IO_3)_3$, has the smallest band gap (2.1 eV) amongst the studied iodates reported in the literature [15]. We also explained the observed pressure-induced band-gap evolution in the same material [15]. By comparing the band gap of $Fe(IO_3)_3$ with that of other metal iodates reported in the literature, we have established that the main factor narrowing the band-gap width in transition-metal iodates is the contribution of partially filled d states from the transition metals to either the valence-band maxima (VBM) or conduction-band minima (CBM) [15]. In contrast, in nontransition or closed-shelled transition-metal iodates, the VBM and CBM are dominated by contributions from O-2p and I-5p orbitals and band-gap energies are generally larger.

Since the conclusions of our previous study [15] suggest that transition metals are best avoided if you wish to engineer a wide band gap, we have moved the focus of our research to the study of nontransition (Mg) and closed-shelled transition metal (Zn) iodates: $Mg(IO_3)_2$ and $Zn(IO_3)_2$. There are some advantages to choosing $Mg(IO_3)_2$ and $Zn(IO_3)_2$ as representative metal iodates: (i) Their high-pressure behaviors, including crystal structures, equations of state, pressure-induced phase transitions, and atomic vibrations have been well characterized and reported [16,17]. This enables us to analyze the pressure-induced band-gap changes of $Mg(IO_3)_2$ and $Zn(IO_3)_2$ from the perspective of the crystal structure, using available information on the iodine-oxygen bond distance. (ii) Their chemical formulas are simple and they are

*daniel.errandonea@uv.es

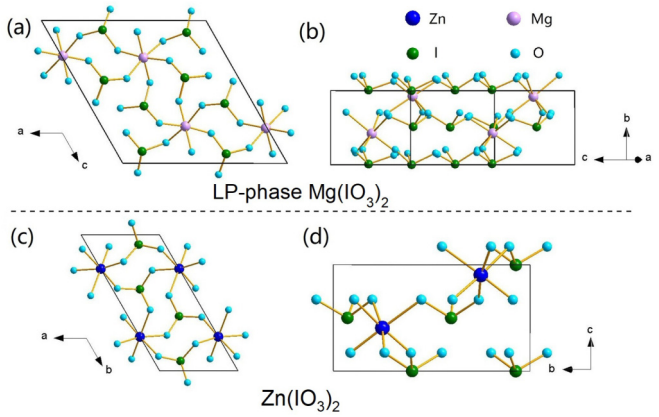

FIG. 1. The crystal structure of the low-pressure (LP) phase of $Mg(IO_3)_2$ projected (a) along the *b* axis and (b) along the *ac* plane, approximately along the *a* axis, to emphasize the layered structure. The crystal structure of the LP phase of $Zn(IO_3)_2$ projected (c) along the *c* axis and (d) along the *a* axis. Pink, dark blue, green, and light blue spheres represent Mg, Zn, I, and O atoms, respectively.

isostructural. Both compounds have related crystal structures, which facilitates comparison to find the factor which governs the band gap. (iii) Their bulk moduli are small, 22.2 GPa [17] and 21.6 GPa [16] for $Mg(IO_3)_2$ and $Zn(IO_3)_2$, respectively. Therefore, the application of pressures smaller than 20 GPa can cause significant changes in the crystal structure, resulting in observable changes in the band gap.

At ambient pressure, both $Mg(IO_3)_2$ and $Zn(IO_3)_2$ crystallize in monoclinic crystal structures (space group: $P2_1$). They are represented in Fig. 1. The main difference between the structures in Fig. 1 is the fact that the crystallographic *a* axis of $Zn(IO_3)_2$ doubles in length to become the same axis of $Mg(IO_3)_2$. In Figs. 1(a) and 1(c) it can be seen that Zn and Mg are each coordinated by six oxygen atoms forming an octahedron. Additionally, in both compounds, iodine is bonded to three oxygen atoms, forming a trigonal pyramid. The metal octahedra, MO_6, and iodate units, $[IO_3]^-$, are connected to each other by corner-sharing oxygen atoms, and the metal octahedra are linked to each other by two $[IO_3]^-$ units. When viewed along the *a* axis, $Mg(IO_3)_2$ [Fig. 1(b)] and $Zn(IO_3)_2$ [Fig. 1(d)], can be described by structures formed by layered $[IO_3]^-$ units [the $Mg(IO_3)_2$ structure in Fig. 1(b) has been rotated slightly around the *b* axis to better show the layered structure]. Each of the $[IO_3]^-$ units has a lone electrons pair (LEP) from the iodine atom which points towards the opposite side of the base of the pyramid [8], i.e., towards the neighboring layer. This LEP orientation means that the interlayer distance is easily reduced under compression. Consequently, upon compression the distance between the iodine atoms and their second-nearest neighboring oxygen atoms is reduced, leading to a gradual increase in the coordination number of iodine and the suppression of the LEPs [16,17]. In order to accommodate the new I–O bonds, the length of the original in-layer iodine-oxygen bonds slightly increases under compression [16,17]. This behavior has been concluded as a common feature of the metal iodates under pressure [16–21], and it leads to the occurrence of subtle phase transitions, which do not exhibit volume discontinuities. As we previously reported [17], $Zn(IO_3)_2$ remains monoclinic up to 27 GPa, but $Mg(IO_3)_2$ transforms from the monoclinic crystal structure (space group: $P2_1$, LP phase) to a trigonal structure (space group: $P3$, HP phase) in a pressure range from 7.5 to 9.7 GPa. The phase transition was characterized by the means of high-pressure synchrotron x-ray diffraction, Raman scattering, the infrared spectroscopy experiments, and first-principle calculations. The structures of both the LP and HP phases were obtained from the refinement of the polycrystalline x-ray diffraction data collected at ambient pressure and high pressures, respectively. As we show later in the present work, the band gaps of these metal iodates change continuously under compression even across the phase transitions.

In this paper we report a two-step investigation into the high-pressure behavior of the electronic band gap of nontransition and closed-shelled transition-metal iodates. In the first step, we determine the band-gap energies of $Mg(IO_3)_2$ and $Zn(IO_3)_2$ under compression up to 18 GPa via optical absorption experiments. The results are compared with results we obtained from first-principle calculations. An analysis of the change of iodine-oxygen bond distances has been used to explain the observed band-gap changes under compression. In the second step, we collate and compare the band-gap energies and corresponding average iodine-oxygen bond distances of the metal iodates reported in the literature. In the comparison, only nontransition and closed-shelled transition metals were included, without regard for their chemical formula, crystal structure, or stoichiometry. The validation of our conclusions provides a rational criterion for designing metal iodates with band-gap energies tailored for applications.

II. EXPERIMENT AND CALCULATION DETAILS

A. Sample synthesis

Zinc chloride (99.9%, CDH), potassium iodate (99%, Merck), and sodium meta silicate nanohydrate (Na_2SiO_3 $9H_2O$, CDH) were used as the starting materials for synthesizing zinc iodate crystals. High-quality single crystals of zinc iodate were grown by single-diffusion gel technique at room temperature and hydrosilica gel was used as the medium of crystal growth. Gel of predetermined specific gravity 1.03–1.05 g/cc was prepared by dissolving the required amount of sodium meta silicate (SMS) in bidistilled water. The amount of potassium iodate corresponding to 0.5 M was dissolved in the SMS. The resulting gel was acidified with glacial acetic acid to obtain a pH in the range 4–7. The resulting solution was transferred into the sides of test tubes with internal diameter 2.5 cm and length 20 cm to avoid air bubbles in the gel medium and to keep the medium undisturbed for gelation. An aqueous solution of zinc chloride was poured slowly over the set gel to prevent gel breakage. The zinc ions slowly diffuse through the narrow pores of the hydrosilica gel and react with the iodate ions present in the gel leading to the formation of high-quality, white zinc iodate single crystals over a time period of 3 weeks.

The polycrystalline $Mg(IO_3)_2$ used in the present work is the same as used in our previous work [17]. While the synthesis method is summarized here, sample purity and crystal structure information can be found in Ref. [17].

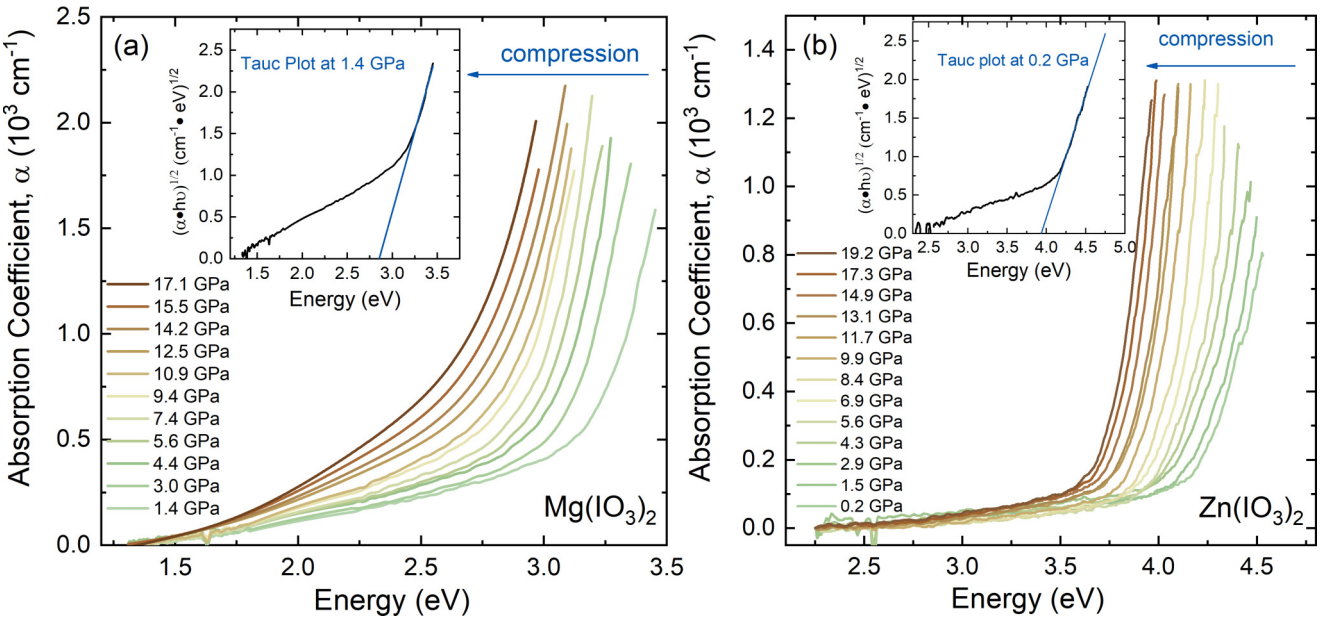

FIG. 2. Optical absorption spectra of (a) $Mg(IO_3)_2$ and (b) $Zn(IO_3)_2$ at selected pressures. The insets are the Tauc plots at the lowest pressure.

Polycrystalline $Mg(IO_3)_2$ was synthesized by adding potassium iodate (99.5% purity, Sigma-Aldrich) dissolved into concentrated nitric acid (2 mmol of KIO_3 in 10 mL of 7N nitric acid) to anhydrous magnesium chloride (98% purity, Sigma-Aldrich) dissolved in concentrated nitric acid (1 mmol in 10 mL of 7N nitric acid). The mixture was thoroughly stirred and then the solvents were left to slowly evaporate for a few days at 60 °C.

B. Optical absorption experiments under high pressure

Membrane-type diamond-anvil cells have been used to generate the high-pressure sample environment. The polycrystalline $Mg(IO_3)_2$ sample was first pressed into compact transparent 20-μm-thick platelets, and for the single crystal $Zn(IO_3)_2$, a piece of sample with a thickness around 20 μm was selected. In two separate experiments, the sample was loaded in 200-μm-diameter holes drilled in a stainless-steel gasket which has been precompressed to a thickness of 45 μm. A mixture of methanol, ethanol, and water in a ratio of 16:3:1 was used as the pressure transition medium (PTM) in the experiment of $Zn(IO_3)_2$. For $Mg(IO_3)_2$, the solid potassium bromide (KBr) was used as PTM in the high-pressure optical absorption experiment, as it can provide quasihydrostatic environment up to 11 GPa [22] and it is transparent in a wide range from 0.23 to 23 μm [23]. In all the experiments, the ruby fluorescence method was employed for pressure calibration [24]. [See the completeness of the loading for those two samples found in the inserted optical micrographs in Figs. 3(a) and 3(b).]

The sample-in and sample-out method was used to acquire the optical absorption spectra at each pressure, in which the intensity of the light transmitted through the sample [$I(\omega)$] was normalized against the intensity of the light transmitted through the PTM [$I_0(\omega)$]. The experiment was conducted on a bespoke optical setup consisting of a tungsten lamp, fused silica lenses, reflecting optics objectives, and a visible near-IR spectrometer (Ocean Optics Maya2000 Pro). More details can be found in earlier works [13,25].

C. Calculation details

Ab initio simulations were carried out within the framework of density-functional theory (DFT) [26], with the Vienna *Ab initio* Simulation Package (VASP) [27]. The projector augmented-wave and pseudopotentials were employed and the plane-wave kinetic cutoff was extended up to 540 eV to ensure highly converged results. The exchange-correlation energy was described within the generalized gradient approximation (GGA) with the Perdew-Burke-Ernzerhof (PBE) for solids prescription (PBEsol) [28]. The integrations over the Brillouin zone (BZ) were carried out with a dense k-point grid as described in Ref. [16] for $Zn(IO_3)_2$. For $Mg(IO_3)_3$ the integrations over the BZ were performed with a $6 \times 4 \times 6$ sampling of k-special points. At selected volumes, the structures we adopted for Mg and Zn iodates were fully relaxed to their optimized configuration through the calculation of the force and the stress tensor. Not only the calculated equilibrium lattice parameter at ambient condition, but also the pressure dependence of the lattice parameter and equation of state show good agreement with that obtained from experiment both for $Mg(IO_3)_2$ [17] and $Zn(IO_3)_2$ [16]. The electronic band-structure calculations were performed using the k path chosen with the SEEK-PATH tool [29], and the band-structure analysis was carried out with the SUMO package [30]. The crystal orbital overlap population (COOP) calculations were performed using the LOBSTER software [31].

III. RESULTS AND DISCUSSION

A. Band-gap energy under compression

Absorption spectra of $Mg(IO_3)_2$ and $Zn(IO_3)_2$ at selected pressures are shown in Figs. 2(a) and 2(b), respectively. Their

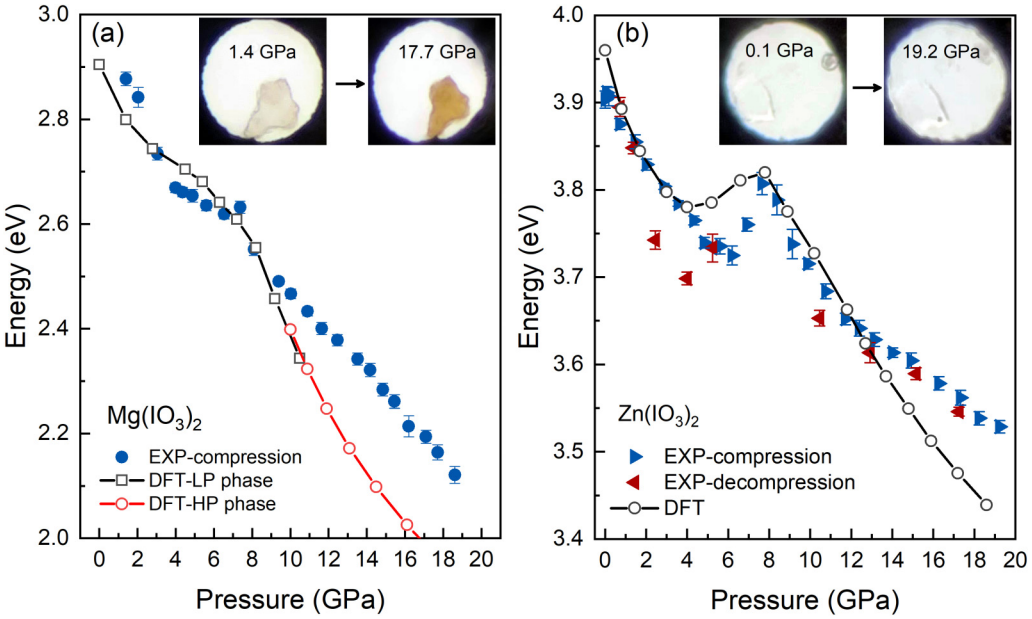

FIG. 3. Pressure dependence of the band-gap energy of (a) $Mg(IO_3)_2$ and (b) $Zn(IO_3)_2$. The experimental results (EXP) are shown with symbols only. The calculated results (DFT) are shown with solid lines and symbols. The insets include optical micrographs showing the sample loaded in the diamond-anvil cell at the indicated pressures. In (a) the theoretical calculated band gap of $Mg(IO_3)_2$ has been shifted by -0.5 eV. In (b) the theoretical calculated band gap of $Zn(IO_3)_2$ has been shifted by $+1.0$ eV.

absorption edges exhibit a gradual redshift with increasing pressure. According to the calculated electronic band structures (Supplemental Material, Fig. S1 [32]) $Mg(IO_3)_2$ and $Zn(IO_3)_2$ are indirect band-gap semiconductors. A Tauc plot analysis for indirect band-gap materials has been used here to obtain the band-gap energy at each pressure by extrapolating the linear fit of the high-energy part of the $(\alpha h\upsilon)^{1/2}$ vs $h\upsilon$ plot to zero [33], where α is the absorption coefficient, h is the Planck constant, and υ is the photon frequency. Examples of the Tauc fits are given in the insets of Figs. 2(a) and 2(b).

At ambient pressure the band gap of $Zn(IO_3)_2$ is 3.90(1) eV (2.96 eV) according to experiments (calculations). This value is higher than the previously reported [34] value of 3.53 eV (2.59 eV) according to experiments (DFT calculations). The difference in observed band-gap energy could be related to (i) different sample thicknesses used for optical absorption experiments [35]. For example, a 20-μm-thick sample was used in the present work, the sample thickness used in the previous study is unknown [34]. It is known that the use of very thick samples can lead to an underestimation of the band-gap energy due to misidentification of Urbach tails as fundamental band-gap absorptions. (ii) According to the calculated electronic band structure, from both this work and Ref. [34], $Zn(IO_3)_2$ has an indirect band gap. However, in Ref. [34], a Tauc plot for direct band-gap materials [25,33] was used.

For $Mg(IO_3)_2$, due to the polycrystalline sample used in our experiments, we could not measure its optical absorption spectra at ambient pressure. However, using the band gap of $Mg(IO_3)_2$ determined at low pressures [see Fig. 3(a)] it is possible to estimate the ambient-pressure band gap by adopting a linear fit to data obtained from 1.4 to 4.4 GPa. The estimated ambient-pressure band gap of $Mg(IO_3)_2$ is 3.00(5) eV. This value is slightly lower than the band-gap value of 3.4 eV obtained from calculations. The underestimation of the calculated band gap in $Zn(IO_3)_2$ and overestimation of the calculated band gap in $Mg(IO_3)_2$ deserves a comment. The discrepancy in $Zn(IO_3)_2$ is typical of DFT calculations and it is related to the GGA-PBEsol approximations used to describe the exchange and correlation energies [36,37]. The underestimation of the band-gap energy is more notorious when transition metals (like Zn) are present in the compound and is mostly explained in the literature in terms of the effects of self-interaction and particularly of the derivative discontinuity of the exchange-correlation energy [38]. However, there are indeed more than a few examples where the band gap is overestimated by DFT [39,40]. $Mg(IO_3)_2$ seems to be within these cases. The reasons for band-gap overestimations are still under debate [41] and they are beyond the scope of this work. It should be noted here that in spite of the discrepancies regarding the absolute value of the band gap at zero pressure, calculations closely reproduce the experimental pressure dependence of the band gap of materials including cobalt iodates [42]. This is also the case of $Zn(IO_3)_2$ and $Mg(IO_3)_2$ as we show in the next section.

The experimental and calculated band-gap energies of $Mg(IO_3)_2$ and $Zn(IO_3)_2$ are shown in Figs. 3(a) and 3(b) as functions of pressure. For a better comparison of the experimental and calculated band-gap energy, we have downshifted the calculated band gap of $Mg(IO_3)_2$ by 0.5 eV and upshifted the calculated band gap of $Zn(IO_3)_2$ by 1.0 eV. The band gaps of both compounds decrease under compression and exhibit a nonlinear pressure dependence. For $Mg(IO_3)_2$, there are slope changes around 3 and 8 GPa. We also noticed that the band gap does not show a discontinuity at the structural phase transition pressure 9 GPa. This fact is consistent with the gradual changes associated with the transition. Under pressure, the band-gap energy exhibits a reduction of 29.3%, from 3.00 eV

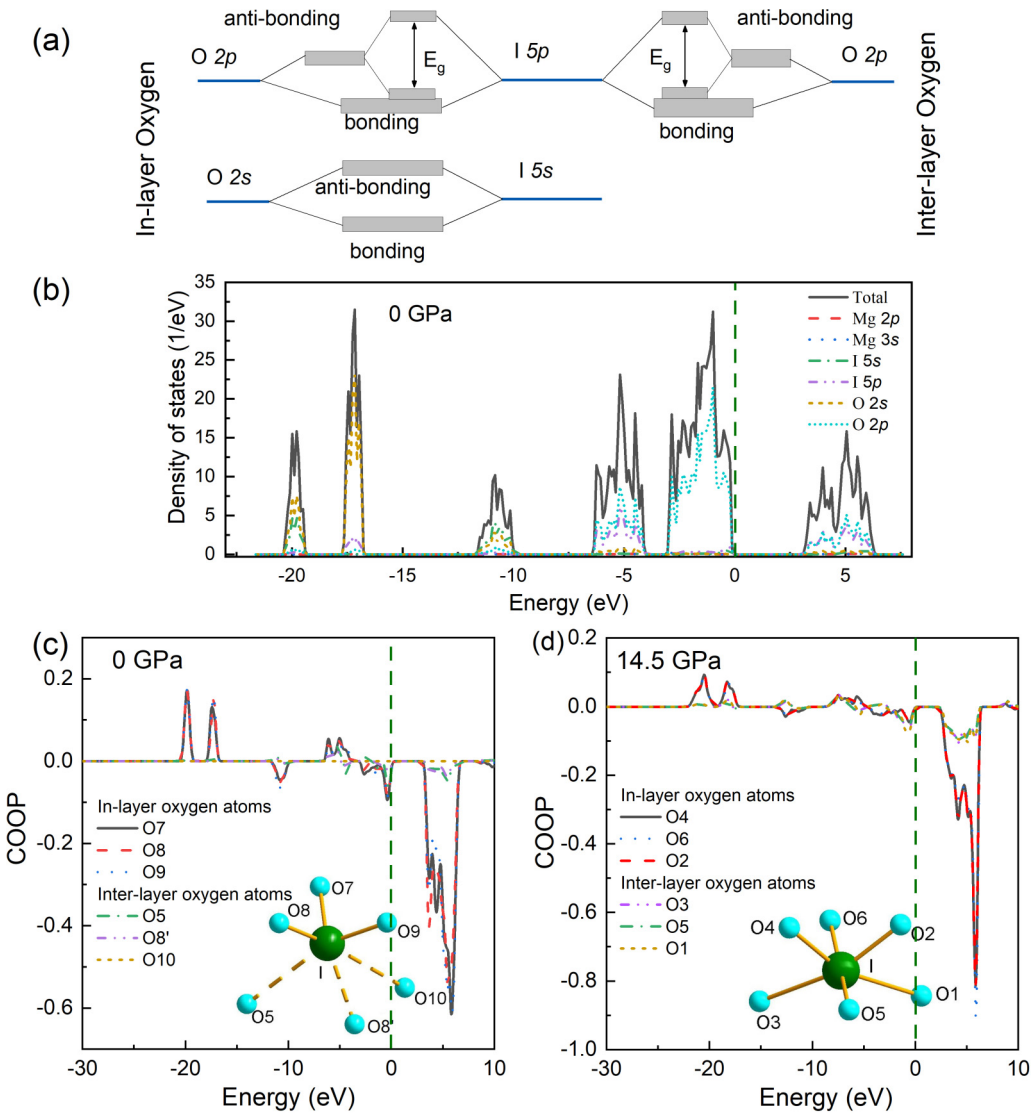

FIG. 4. (a) Molecular orbital diagrams for $Mg(IO_3)_2$ and $Zn(IO_3)_2$ at ambient pressure; here, E_g represents band-gap energy. (b) Calculated DOS and PDOS for $Mg(IO_3)_2$. (c) Calculated COOP for $Mg(IO_3)_2$ at 0 GPa and (d) at 14.5 GPa. The vertical dashed line shows the Fermi level.

at ambient pressure, to 2.12 eV at 18.6 GPa. As shown in the inset in Fig. 3(a), the color of the $Mg(IO_3)_2$ crystal changed from transparent, with a slightly orange tone, to completely orange. Regarding $Zn(IO_3)_2$, the band-gap behavior is similar, showing a decrease in energy from 3.90 eV at ambient pressure to 3.74 eV at 5.6 GPa according to experiments. In our calculations, the band-gap energy decreases from 2.96 eV at 0 GPa to 2.78 eV at 4 GPa. Upon further compression, band-gap narrowing is followed by a slight broadening of the band gap up to 7.7 GPa. Beyond 7.7 GPa, the band gap shows a continuous narrowing up to the highest pressure covered in this study. The total reduction of the band gap is 9.5% in the experiment. In $Zn(IO_3)_2$ we did not detect any observable color change in the experiments.

B. Molecular orbital diagram

Due to the fact that both $Mg(IO_3)_2$ and $Zn(IO_3)_2$ show qualitatively similar high-pressure behavior of the band-gap energy, we shall use $Mg(IO_3)_2$ as the example in point to discuss the pressure evolution of the band-gap energy in both materials. The calculated density of states (DOS) and projected density of states (PDOS) are provided in Fig. 4(b). The VBM is dominated by O-2p orbitals and the CBM by contributions from O-2p and I-5p orbitals. In this regard, the PDOS is qualitatively similar to those reported for other nontransition-metal iodates [15]. The common feature of dominant contributions from O-2p and I-5p orbitals indicates that the band-gap energy in metal iodates is strongly affected by the I-O interaction. In Figs. 4(c) and 4(d), we show the calculated COOP of $Mg(IO_3)_2$ between iodine and the six nearest oxygen atoms at 0 and 14.5 GPa, respectively. Notably, there are two types of I-O interaction. The first type of I-O interaction is the bonding between iodine and the in-layer oxygen atoms; O8, O7, and O9 in Fig. 4(c). (For clarity, we follow the same labeling convention as provided in the crystallographic information file (CIF) provided by Phanon *et al.* [43]). These I-O bonds are relatively short, typically

from 1.75 to 1.86 Å. The second type of I-O interaction is between iodine and the oxygen atoms in the neighboring $[IO_3]^-$ layer. These interlayer oxygen atoms are O5, O8′, and O10 in Fig. 4(c). These types of bonding are weak or do not exist at low pressure. The distance between the iodine and the interlayer oxygen atoms is from 2.6 to 3.1 Å.

The combination of the PDOS and COOP enables us to determine the molecular orbital (MO) diagram of $Mg(IO_3)_2$ [Fig. 4(a)]. In the −20 to −17 eV energy region, the DOS and PDOS of $Mg(IO_3)_2$ [Fig. 4(b)] are dominated by I-5*s* and O-2*s* states. Both of them are positive in COOP [Fig. 4(c)] for the in-layer oxygen atoms, and both are almost zero for the interlayer oxygen. The energy region around −10 eV in PDOS is contributed to mainly by I-5*s* and O-2*s* states. The contribution to the COOP is negative for in-layer oxygen atoms and zero for interlayer oxygen atoms. These two energy regions correspond to the bonding and antibonding states between I-5*s* and O-2*s* [as illustrated in the bottom left part of Fig. 4(a)]. There are also two broad bands located between −7 eV and the top of the valence band. The lower-energy band is dominated by O-2*p* and I-5*p* orbitals and the corresponding contribution to the COOP is positive, which means these orbitals belong to the bonding state of the *p*-*p* interaction between iodine and oxygen [see the left-hand part of Fig. 4(a)]. The antibonding state of these *p* orbitals is at the bottom of the conduction band, which is primarily contributed to by the O-2*p* and I-5*p* states and shows a negative COOP. Based on this description, and the fact that the top of the valence band is also dominated by nonbonding O-2*p* states, we construct the MO diagram (for the −8 to 6 eV energy region) provided in Fig. 4(a). In this energy range, the COOP indicates only a minor interaction but the same characteristics between iodine and the interlayer oxygen atoms. Therefore, we suggest the same MO diagram for the *p*-*p* interaction between iodine and the interlayer oxygen atoms [the top right part in Fig. 4(a)]. The band-gap energy is given by the energy between the oxygen nonbonding state and the *p*-*p* antibonding state between iodine and oxygen. At high pressures, taking 14.5 GPa as an arbitrary example above the phase transition pressure (9 GPa [17]), the interaction between iodine and interlayer oxygen atoms is enhanced at the conduction band and the upper part of the valence band due to the compression of the interlayer distance. The COOPs at 0 and at 14.5 GPa share very similar characteristics [Figs. 4(c) and 4(d)] and can be used to determine essentially similar MO diagrams. Only minor differences are observed: for example, at 14.5 GPa the iodine and the interlayer oxygen atoms have small amount of contribution to the lower-energy region; however, the overall characterization is the same.

In Fig. 5 we have plotted the calculated pressure dependence of the bond distances between iodine and in-layer/interlayer oxygen atoms [17]. These I-O distances are taken from our DFT calculations, which show good agreement with our experimental results regarding crystallographic lattice parameters (determined from powder x-ray diffraction) and their pressure evolution (via the P/V equation of state). The distance between iodine and interlayer oxygen atoms (O5, O8′, and O10 in the LP phase) shortens under compression. In contrast, the bond distance between iodine and the in-layer oxygen atoms (O7, O8, and O9) slightly

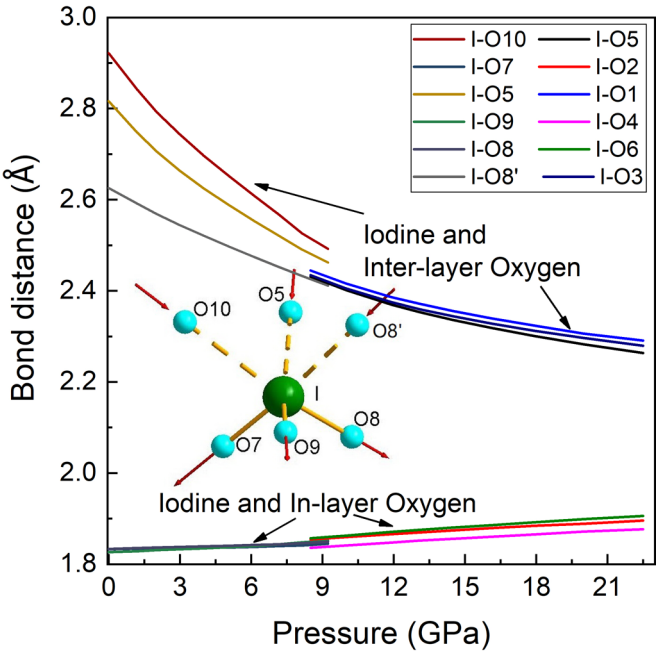

FIG. 5. Calculated pressure dependence of the bond distance between iodine and the in-layer/interlayer oxygen atoms in $Mg(IO_3)_2$. The slight discontinuity at around 9 GPa is due to a phase transition.

enlarges under compression. Due to the stereoactive LEP on iodine, and the shortening of the distance between iodine and interlayer oxygen atoms, new I-O bonds form between them on compression. Consequently, the in-layer oxygen atoms are pushed away from iodine. This is a typical behavior observed in metal iodates under compression [16–18,21] as discussed in the Introduction. Therefore, there are two competing effects which determine the pressure evolution of the band-gap energy of $Mg(IO_3)_2$. The first effect (effect 1) is the enlargement of the I-O bond distance between iodine and in-layer oxygen atoms which results in a decrease of the hybridization between their orbitals, thereby decreasing the energy difference between their bonding and antibonding states. As a consequence, the band-gap energy will tend to decrease with increasing pressure. The second effect (effect 2) is the shortening of the distance between iodine and the interlayer oxygen atoms which increases the hybridization between their states and increase the separation between bonding and antibonding states, thereby favoring an increase in the band-gap energy.

In the case of $Mg(IO_3)_2$, below 4 GPa the interaction between iodine and the interlayer oxygen atoms is weak due to the large interlayer distance. Therefore, the interaction between iodine and the closer in-layer oxygen atoms dominates the band gap. Since the in-layer I-O distances increase with increasing pressure, the band-gap energy consequently decreases with increasing pressure. In other words, effect 1 is dominant below 4 GPa. From 4 to 8 GPa the distance between iodine and the interlayer oxygen atoms quickly gets shorter, thereby enhancing their mutual interaction and counteracting the narrowing of the band gap. In other words, there is competition between effects 1 and 2 between 4 and 8 GPa, but effect 2 dominates because the interlayer I-O bond distance is more sensitive to pressure. Above 8 GPa, the shortening

of the interlayer I-O bond distance becomes less sensitive to pressure (see Fig. 5). Therefore, the increasing in-layer I-O distance (effect 1) once again dominates the pressure dependence of the band-gap energy, which continues to decrease above 8 GPa up to the maximum pressure studied in the present work. The high-pressure band-gap behavior of $Zn(IO_3)_2$ can also be explained following the same rationale and by the same MO diagram. (The $Zn(IO_3)_2$ DOS, PDOS, and pressure dependence of the distance between iodine and in-layer/interlayer oxygen atoms can be found in Figs. S2 and S3 in the Supplemental Material [32], respectively.) Notice that both compounds exhibit a qualitatively similar pressure dependence for the band-gap energy. The differences in the pressure dependence of the band-gap energy (see Fig. 3) are a consequence of the difference in the pressure evolution of both crystal structures (which are similar but not identical) under compression, as we have shown in our previous works [16,17]. Our conclusions indicate that wide band-gap metal iodates can be designed based on crystal structures which contain iodate molecules with short iodine-oxygen bond distances.

It is worth mentioning here that the MO model we suggested can only qualitatively explain the band-gap behavior of nontransition or closed-shell transition-metal iodates. Indeed, the band-gap energies for different metal iodates exhibit different sensitivities to the I-O bond distance, although the trend is the same, i.e., the band-gap energy decreases as the average I-O distance increases. According to the theoretical calculated band-gap energy and I-O bond distance for Zn and Mg iodates at the pressure range from 0 to 18 GPa, the band-gap energy decreases with the I-O bond distance by 8 and 31 eV/Å, respectively, thereby exhibiting different pressure dependences which are not explained by our model. The corresponding value for all the data shown in Fig. 6, where we summarized the band-gap energy and average I-O bond distance for 71 different metal iodates at ambient condition, is −42 eV/Å.

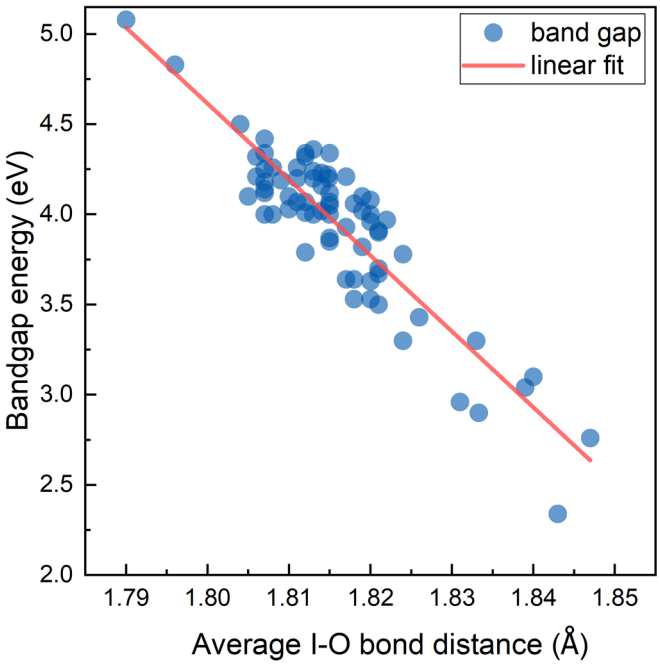

FIG. 6. Collated band-gap energy and average I-O bond distances as found in the literature. The detailed information for each point, including chemical fromula, average I-O bond distance, and band-gap energy for the compounds, can be found in Fig. S5 and Table S1 in Supplemental Material [32].

C. Metal iodate band gaps at ambient pressure

It is worth examining the relationship between the iodine-oxygen bond distances and the band-gap energies we found in Mg and Zn iodates by making comparison with other metal iodates. In Fig. 6 we have plotted the band-gap energy vs the average I-O bond distance of the metal iodates measured in this work and reported in the literature [1–3,10–12,16,43–82] (see Figs. S4 and S5 in the Supplemental Material [32]). In the comparison, only nontransition and closed-shelled transition metal iodates were included, without regard for their chemical formula, crystal structure, or stoichiometry. Partial-filled transition-metal iodates were not included because in those iodates the 3*d* electrons also contribute to the electronic states near the Fermi level [15]. The average I-O bond was calculated by considering bond distances shorter than the cutoff value of 2.0 Å. The choice of the cutoff value is based on the fact that the interaction between iodine and oxygen is weak when the oxygen is further than 2.0 Å away from iodine (see Fig. 5). The band-gap energy of the metal iodates ranges from 2.34 eV in $K_8Ce_2I_{18}O_{53}$ [44] to 5.08 eV in $Rb_3(IO_3)_3(I_2O_5)(HIO_3)_4(H_2O)$ [45], and the average I-O bonds varies from 1.79 to 1.84 Å. In Fig. 6 it can be seen that there is a negative correlation between the average iodine-oxygen bond distance and the band-gap energy of metal iodates. This is a reasonable result because the electronic structure of the metal iodates has a common characteristic near the Fermi level. That is, the VBM is dominated by the O-2*p* orbital, while the CBM is contributed to by the O-2*p* and I-5*p* orbitals, which indicates that the band-gap energy is dominated by the interaction between the iodine and oxygen atoms, and that the metal species is not the dominant factor. According to the MO diagram we suggested for Mg and Zn iodates in the previous part, their band-gap energies decrease with increasing bond distance between iodine and the in-layer oxygen atoms. Therefore, the band gap of nontransition or closed-shelled metal iodates have a negative correlation with the bond distance, regardless of crystal structure, metal species, or chemical formula.

IV. CONCLUSIONS

The main conclusion from the first half of the present work is that the band-gap energy of the studied iodates [nontransition (Mg) and closed-shell transition-metal (Zn) iodates: $Mg(IO_3)_2$ and $Zn(IO_3)_2$] is strongly related to the distance between the iodine and in-layer/interlayer oxygen atoms. Through the analysis of the experimental band-gap energy as a function of pressure, combined with the help of calculated density of states, projected density of states, and calculated crystal orbital overlap populations between the iodine and oxygen atoms, we conclude that there are two competing effects regarding the I-O bond distances. Firstly, the pressure-induced enlargement of the bond distance between iodine and in-layer oxygen atoms reduces their mutual interaction

and thereby causes a narrowing of the band gap. Secondly, hybridization between iodine and interlayer oxygen atoms causes opening of the band gap. The competition between these two effects causes the nonlinear reduction of the band-gap energy with increasing pressure.

The main conclusion from the second half of the present work, in which we examine the band-gap energies and average I-O bond distances of 71 different nontransition or closed-shelled transition-metal iodates reported in the literature, is that we find the band-gap energy in iodate materials to have a negative correlation with the average I-O bond distance regardless of chemical formula, crystal structure, metal species, or iodine coordination number. This observation is consistent with the model proposed in the first half of the present work to explain the high-pressure behavior of the band-gap energy of Mg and Zn iodates. Combining our previous work [15] on the high-pressure band-gap studies on transition-metal iodates, $Fe(IO_3)_3$, we thereby find two useful rules for designing wide band-gap metal iodates: (i) do not use partially filled transition-metal iodates because their $3d$ electrons contribute to the electronic states near the Fermi level [15], and, (ii) the shorter the bond distance between iodine and nearest oxygen, the wider the band gap of the metal iodate.

ACKNOWLEDGMENTS

This work was supported by the Generalitat Valenciana under Grant No. PROMETEO 2018/123-EFIMAT and by the Spanish Ministerio de Ciencia e Innovación and Agencia Estatal de Investigación (Grant No. MCIN/AEI/10.13039/501100011033) and the European Union under Grants No. PID2019-106383GB-41/43 and No. RED2018-102612-T (MALTA Consolider Team). A.L. and D.E. thank the Generalitat Valenciana for the Ph.D. Fellowship No. GRISOLIAP/2019/025. R.T. acknowledges funding from the Spanish MINECO via Juan de la Cierva Formación program (Grant No. FJC2018-036185-I).

[1] H. Fan, G. Peng, C. Lin, K. Chen, S. Yang, and N. Ye, $Ba(IO_3)F$: An alkaline-earth-metal iodate fluoride crystal with large band gap and birefringence, Inorg. Chem. **59**, 7376 (2020).

[2] H. Jo, H. G. Kim, H. R. Byun, J. I. Jang, and K. M. Ok, Synthesis, structure, and third-harmonic generation measurements of a mixed alkali metal iodate, $KLi_2(IO_3)_3$, J. Solid State Chem. **282**, 121120 (2020).

[3] F. F. Mao, C. L. Hu, J. Chen, B. L. Wu, and J. G. Mao, $HBa_{2.5}(IO_3)_6(I_2O_5)$ and $HBa(IO_3)(I_4O_{11})$: Explorations of second-order nonlinear optical materials in the alkali-earth polyiodate system, Inorg. Chem. **58**, 3982 (2019).

[4] H. Liu, X. Jiang, X. Wang, L. Yang, Z. Lin, Z. Hu, X. Meng, X. Chen, and J. Qin, Influence of A-site cations on germanium iodates as mid-IR nonlinear optical materials: $A_2Ge(IO_3)_6$ (A = Li, K, Rb and Cs) and $BaGe(IO_3)_6 \cdot H_2O$, J. Mater. Chem. C **6**, 4698 (2018).

[5] X. Xu, C. Hu, B. Li, B. Yang, and J. Mao, α-AgI_3O_8 and β-AgI_3O_8 with large SHG Responses: Polymerization of IO_3 groups into the I_3O_8 polyiodate anion, Chem. Mater. **26**, 3219 (2014).

[6] L. Xiao, Z. Cao, J. Yao, Z. Lin, and Z. Hu, A new cerium iodate infrared nonlinear optical material with a large second-harmonic generation response, J. Mater. Chem. C **5**, 2130 (2017).

[7] J. Yeon, S. H. Kim, and P. S. Halasyamani, New thallium iodates-synthesis, characterization, and calculations of $Tl(IO_3)_3$ and $Tl_4(IO_3)_6$, $[Tl^+{}_3Tl^{3+}(IO_3)_6]$, J. Solid State Chem. **182**, 3269 (2009).

[8] H. Y. Chang, S. H. Kim, M. O. Kang, and P. S. Halasyamani, Polar or nonpolar? A^+ cation polarity control in $A_2Ti(IO_3)_6$ (A = Li, Na, K, Rb, Cs, Tl), J. Am. Chem. Soc. **131**, 6865 (2009).

[9] T. Abudouwufu, M. Zhang, S. Cheng, H. Zeng, Z. Yang, and S. Pan, $K_2Na(IO_3)_2(I_3O_8)$ with strong second harmonic generation response activated by two types of isolated iodate anions, Chem. Mater. **32**, 3608 (2020).

[10] F. F. Mao, C. L. Hu, J. Chen, and J. G. Mao, A series of mixed-metal germanium iodates as second-order nonlinear optical materials, Chem. Mater. **30**, 2443 (2018).

[11] Q. Wu, H. Liu, F. Jiang, L. Kang, L. Yang, Z. Lin, Z. Hu, X. Chen, X. Meng, and J. Qin, $RbIO_3$ and $RbIO_2F_2$: Two promising nonlinear optical materials in mid-IR region and influence of partially replacing oxygen with fluorine for improving laser damage threshold, Chem. Mater. **28**, 1413 (2016).

[12] Q. M. Huang, C. L. Hu, B. P. Yang, Z. Fang, Y. Lin, J. Chen, B. X. Li, and J. G. Mao, $[GaF(H_2O)][IO_3F]$: A promising NLO material obtained by anisotropic polycation substitution, Chem. Sci. **12**, 9333 (2021).

[13] D. Errandonea, C. Popescu, A. B. Garg, P. Botella, D. Martinez-García, J. Pellicer-Porres, P. Rodríguez-Hernández, A. Muñoz, V. Cuenca-Gotor, and J. A. Sans, Pressure-induced phase transition and band-gap collapse in the wide-band-gap semiconductor $InTaO_4$, Phys. Rev. B **93**, 035204 (2016).

[14] E. Bandiello, D. Errandonea, D. Martinez-Garcia, D. Santamaria-Perez, and F. J. Manjón, Effects of high-pressure on the structural, vibrational, and electronic properties of Monazite-type $PbCrO_4$, Phys. Rev. B **85**, 024108 (2012).

[15] A. Liang, P. Rodríguez-Hernandez, A. Munoz, S. Raman, A. Segura, and D. Errandonea, Pressure-dependent modifications in the optical and electronic properties of $Fe(IO_3)_3$: The Role of Fe 3d and I 5p lone-pair electrons, Inorg. Chem. Front. **8**, 4780 (2021).

[16] A. Liang, C. Popescu, F. J. Manjon, A. Muñoz, Z. Hebboul, and D. Errandonea, Structural and vibrational study of $Zn(IO_3)_2$ Combining high-pressure experiments and density-functional theory, Phys. Rev. B **103**, 054102 (2021).

[17] A. Liang, R. Turnbull, C. Popescu, F. J. Manjón, E. Bandiello, A. Muñoz, I. Yousef, Z. Hebboul, and D. Errandonea, Pressure-induced phase transition and increase of oxygen-iodine coordination in magnesium iodate, Phys. Rev. B **105**, 054105 (2022).

[18] A. Liang, C. Popescu, F. J. Manjon, R. Turnbull, E. Bandiello, P. Rodriguez-Hernandez, A. Muñoz, I. Yousef, Z. Hebboul, and

D. Errandonea, Pressure-driven symmetry-preserving phase transitions in $Co(IO_3)_2$, J. Phys. Chem. C **125**, 17448 (2021).

[19] D. Jiang, H. Song, T. Wen, Z. Jiang, C. Li, K. Liu, W. Yang, H. Huang, and Y. Wang, Pressure-driven two-step second-harmonic-generation switching in $BiOIO_3$, Angew. Chem. Int. Ed. **61**, e202116656 (2022).

[20] H. Song, D. Jiang, N. Wang, W. Xing, R. Guo, Z. Lin, J. Yao, Y. Wang, H. Tu, and G. Zhang, $Na_3Bi(IO_3)_6$: An alkali-metal bismuth iodate with intriguing one-dimensional $[BiI_6O_{18}]$ chains and pressure-induced structural transition, Inorg. Chem. **60**, 2893 (2021).

[21] A. Liang, S. Rahman, H. Saqib, P. Rodriguez-Hernandez, A. Munoz, G. Nenert, I. Yousef, C. Popescu, and D. Errandonea, First-order isostructural phase transition induced by high pressure in $Fe(IO_3)_3$, J. Phys. Chem. C **124**, 8669 (2020).

[22] A. Celeste, F. Borondics, and F. Capitani, Hydrostaticity of pressure-transmitting media for high pressure infrared spectroscopy, High Press. Res. **39**, 608 (2019).

[23] E. D. Palik, *Handbook of Optical Constants of Solid* (Academic Press, Maryland, 1997).

[24] H. K. Mao, J. Xu, and P. M. Bell, Calibration of the ruby pressure gauge to 800 Kbar under quasi-hydrostatic conditions, J. Geophys. Res. **91**, 4673 (1986).

[25] O. Gomis, R. Vilaplana, F. J. Manjón, J. Ruiz-Fuertes, E. Pérez-González, J. López-Solano, E. Bandiello, D. Errandonea, A. Segura, P. Rodríguez-Hernández, A. Muñoz, V. V. Ursaki, and I. M. Tiginyanu, $HgGa_2Se_4$ under high pressure: An optical absorption study, Phys. Status Solidi Basic Res. **252**, 2043 (2015).

[26] P. Hohenberg and W. Kohn, Inhomogeneous electron gas, Phys. Rev. **136**, B864 (1964).

[27] G. Kresse and J. Furthmüller, Efficient iterative schemes for ab initio total-energy calculations using a plane-wave basis set, Phys. Rev. B **54**, 11169 (1996).

[28] J. P. Perdew, A. Ruzsinszky, G. I. Csonka, O. A. Vydrov, G. E. Scuseria, L. A. Constantin, X. Zhou, and K. Burke, Restoring the Density-Gradient Expansion for Exchange in Solids and Surfaces, Phys. Rev. Lett. **100**, 136406 (2008).

[29] Y. Hinuma, G. Pizzi, Y. Kumagai, F. Oba, and I. Tanaka, Band structure diagram paths based on crystallography, Comput. Mater. Sci. **128**, 140 (2017).

[30] A. M. Ganose, A. J. Jackson, and D. O. Scanlon, Sumo: Command-line tools for plotting and analysis of periodic ab initio calculations, J. Open Source Softw. **3**, 717 (2018).

[31] S. Maintz, V. L. Deringer, A. L. Tchougréeff, and R. Dronskowski, LOBSTER: A tool to extract chemical bonding from plane-wave based DFT, J. Comput. Chem. **37**, 1030 (2016).

[32] See Supplemental Material at http://link.aps.org/supplemental/10.1103/PhysRevMaterials.6.044603 for additional information on calculated electronic structure and literature search for the band gap of metal iodates analysis (n.d.).

[33] J. Tauc, Optical properties and electronic structure of amorphous Ge and Si, Mater. Res. Bull. **3**, 37 (1968).

[34] A. Benghia, Z. Hebboul, R. Chikhaoui, I. khaldoun Lefkaier, A. Chouireb, and S. Goumri-Said, Effect of iodic acid concentration in preparation of zinc iodate: Experimental characterization of $Zn(IO_3)_2$, and its physical properties from density functional theory, Vacuum **181**, 109660 (2020).

[35] J. P. Enríquez and X. Mathew, Influence of the thickness on structural, optical and electrical properties of chemical bath deposited CdS thin films, Sol. Energy Mater. Sol. Cells **76**, 313 (2003).

[36] M. K. Y. Chan and G. Ceder, Efficient Band Gap Prediction for Solids, Phys. Rev. Lett. **105**, 196403 (2010).

[37] A. Liang, L. T. Shi, S. Gallego-parra, O. Gomis, D. Errandonea, and I. M. Tiginyanu, Pressure-induced band anticrossing in two adamantine ordered-vacancy compounds: $CdGa_2S_4$ and $HgGa_2S_4$, J. Alloys Compd. **886**, 161226 (2021).

[38] J. P. Perdew, W. Yang, K. Burke, Z. Yang, E. K. U. Gross, M. Scheffler, G. E. Scuseria, T. M. Henderson, I. Y. Zhang, A. Ruzsinszky, H. Peng, J. Sun, E. Trushin, and A. Görling, Understanding band gaps of solids in generalized Kohn-Sham theory, Proc. Natl. Acad. Sci. **114**, 2801 (2017).

[39] J. M. Crowley, J. Tahir-Kheli, and W. A. Goddard, Resolution of the band gap prediction problem for materials design, J. Phys. Chem. Lett. **7**, 1198 (2016).

[40] P. Botella, D. Errandonea, A. B. Garg, P. Rodriguez-Hernandez, A. Muñoz, S. N. Achary, and A. Vomiero, High-pressure characterization of the optical and electronic properties of $InVO_4$, $InNbO_4$, and $InTaO_4$, SN Appl. Sci. **1**, 389 (2019).

[41] P. Borlido, J. Schmidt, A. W. Huran, F. Tran, M. A. L. Marques, and S. Botti, Exchange-correlation functionals for band gaps of solids: Benchmark, reparametrization and machine learning, Npj Comput. Mater. **6**, 96 (2020).

[42] A. Liang, F. Rodríguez, A. Muñoz, P. Rodríguez-Hernandez, R. Turnbull, and D. Errandonea, High-pressure tuning of d–d crystal-field electronic transitions and electronic band gap in $Co(IO_3)_2$, Phys. Rev. B **105**, 115204 (2022).

[43] D. Phanon, B. Bentria, E. Jeanneau, D. Benbertal, A. Mosset, and I. Gautier-Luneau, Crystal structure of $M(IO_3)_2$ metal iodates, twinned by pseudo-merohedry, with M^{II}: Mg^{II}, Mn^{II}, Co^{II}, Ni^{II}, and Zn^{II}, Z. Kristallogr. **221**, 635 (2006).

[44] R. Wu, X. Jiang, M. Xia, L. Liu, X. Wang, Z. Lin, and C. Chen, $K_8Ce_2I_{18}O_{53}$: A novel potassium cerium(IV) iodate with enhanced visible light driven photocatalytic activity resulting from polar zero dimensional $[Ce(IO_3)_8]^{4-}$ units, Dalton Trans. **46**, 4170 (2017).

[45] X. Xu, B. Yang, C. Huang, and J. Mao, Explorations of new second-order nonlinear optical materials in the ternary rubidium iodate system: Noncentrosymmetric β-$RbIO_3(HIO_3)_2$ and centrosymmetric $Rb_3(IO_3)_3(I_2O_5)(HIO_3)_4(H_2O)$, Inorg. Chem. **53**, 1756 (2014).

[46] J. K. Liang and C. G. Wang, The structure of $Zn(IO_3)_2$ crystal, Acta Chim. Sin. **40**, 985 (1982).

[47] V. Petříček, K. Malý, B. Kratochvíl, J. Podlahová, and J. Loub, Barium Diiodate, Acta Crystallogr., Sect. B: Struct. Crystallogr. Cryst. Chem. **B36**, 2130 (1980).

[48] S. Ghose, C. Wan, and O. Wittke, The crystal structure of synthetic lautarite, $Ca(IO_3)_2$, Acta Crystallogr., Sect. B **B34**, 84 (1978).

[49] M. Zhang, C. Hu, T. Abudouwufu, Z. Yang, and S. Pan, Functional materials design via structural regulation originated from ions introduction: A study case in cesium iodate system, Chem. Mater. **30**, 1136 (2018).

[50] Y. J. Jia, Y. G. Chen, Y. Guo, X. F. Guan, C. Li, B. Li, M. M. Liu, and X. M. Zhang, $LiM^{II}(IO_3)_3$ (M^{II} = Zn and Cd): Two promising nonlinear optical crystals derived from a tunable structure model of α-$LiIO_3$, Angew. Chemie - Int. Ed. **58**, 17194 (2019).

[51] M. Luo, F. Liang, X. Hao, D. Lin, B. Li, Z. Lin, and N. Ye, Rational design of the nonlinear optical response in a tin iodate fluoride $Sn(IO_3)_2F_2$, Chem. Mater. **32**, 2615 (2020).

[52] D. Phanon and I. Gautier-Luneau, Promising material for infrared nonlinear optics: NaI_3O_8 Salt containing an octaoxotriiodate(V) anion formed from condensation of $[IO_3]^-$ ions, Angew. Chemie - Int. Ed. **46**, 8488 (2007).

[53] Y. Huang, X. Meng, P. Gong, L. Yang, Z. Lin, X. Chen, and J. Qin, A_2BiI_5O ($A = K^+$ or Rb^+): Two new promising nonlinear optical materials containing $[I_3O_9]^{3-}$ bridging anionic groups, J. Mater. Chem. C **2**, 4057 (2014).

[54] S. D. Nguyen, J. Yeon, S. H. Kim, and P. S. Halasyamani, $BiO(IO_3)$: A new polar iodate that exhibits an Aurivillius-type $(Bi_2O_2)^{2+}$ layer and a large SHG response, J. Am. Chem. Soc. **133**, 12422 (2011).

[55] F.-F. Mao, C.-L. Hu, X. Xu, D. Yan, B.-P. Yang, and J.-G. Mao, $Bi(IO_3)F_2$: The first metal iodate fluoride with a very strong second harmonic generation effect, Angew. Chemie **129**, 2183 (2017).

[56] Z. Cao, Y. Yue, J. Yao, Z. Lin, R. He, and Z. Hu, $Bi_2(IO_4)(IO_3)_3$: A new potential infrared nonlinear optical material containing $[IO_4]^{3-}$ anion, Inorg. Chem. **50**, 12818 (2011).

[57] M. Zhang, X. Su, M. Mutailipu, Z. Yang, and S. Pan, $Bi_3OF_3(IO_3)_4$: metal oxyiodate fluoride featuring a carbon-nanotube-like topological structure with large second harmonic generation response, Chem. Mater. **29**, 945 (2017).

[58] T. Hu, L. Qin, F. Kong, Y. Zhou, and J. G. Mao, $Ln_3Pb_3(IO_3)_{13}(\mu^3{-}O)$ (Ln = La−Nd): New types of second-order nonlinear optical materials containing two types of lone pair cations, Inorg. Chem. **48**, 2193 (2009).

[59] J. Chen, C. L. Hu, F. F. Mao, B. P. Yang, X. H. Zhang, and J. G. Mao, REI_5O_{14} (RE = Y and Gd): Promising SHG materials featuring the semicircle-shaped $I_5O_{14}^{3-}$ polyiodate anion, Angew. Chemie - Int. Ed. **58**, 11666 (2019).

[60] F. F. Mao, C. L. Hu, B. X. Li, and J. G. Mao, Acentric $La_3(IO_3)_8(OH)$ and $La(IO_3)_2(NO_3)$: Partial substitution of iodate anions in $La(IO_3)_3$ by hydroxide or nitrate anion, Inorg. Chem. **56**, 14357 (2017).

[61] B. P. Yang, C. F. Sun, C. L. Hu, and J. G. Mao, A series of new alkali metal indium iodates with isolated or extended anions, Dalton Trans. **40**, 1055 (2011).

[62] L. Lin, L. Li, C. Wu, Z. Huang, M. G. Humphrey, and C. Zhang, Incorporating rare-earth cations with moderate electropositivity into iodates for the optimized second-order nonlinear optical performance, Inorg. Chem. Front. **7**, 2736 (2020).

[63] J. Chen, C. L. Hu, F. F. Mao, X. H. Zhang, B. P. Yang, and J. G. Mao, $LiMg(IO_3)_3$: An excellent SHG material designed by single-site aliovalent substitution, Chem. Sci. **10**, 10870 (2019).

[64] S. J. Oh, H. G. Kim, H. Jo, T. G. Lim, J. S. Yoo, and K. M. Ok, Photoconversion mechanisms and the origin of second-harmonic generation in metal iodates with wide transparency, $NaLn(IO_3)_4$ (Ln = La, Ce, Sm, and Eu) and $NaLa(IO_3)_4 : Ln^{3+}$ (Ln = Sm and Eu), Inorg. Chem. **56**, 6973 (2017).

[65] M. Gai, Y. Wang, T. Tong, Z. Yang, and S. Pan, $ZnIO_3F$: Zinc iodate fluoride with large birefringence and wide band gap, Inorg. Chem. **59**, 4172 (2020).

[66] G. Peng, C. Lin, D. Zhao, L. Cao, H. Fan, K. Chen, and N. Ye, $Sr[B(OH)_4](IO_3)$ and $Li_4Sr_5[B_{12}O_{22}(OH)_4](IO_3)_2$: Two unprecedented metal borate-iodates showing a subtle balance of enlarged band gap and birefringence, Chem. Commun. **55**, 11139 (2019).

[67] C. Sun, Y. Wu, D. Mei, and T. Doert, $Bi_2(IO_3)(IO_6)$: First combination of $[IO_3]^-$ and $[IO_6]^{5-}$ anions in three-dimensional framework, Solid State Sci. **77**, 37 (2018).

[68] H. S. Ahn, D. W. Lee, and K. M. Ok, Dimensionality variations in new zirconium iodates: Hydrothermal syntheses, structural determination, and characterization of $BaZr(IO_3)_6$ and $K_2Zr(IO_3)_6$, Dalton Trans. **43**, 10456 (2014).

[69] Y. An, Y. Zhong, T. Sun, H. Wang, Z. Hu, H. Liu, S. Liu, Y. Kong, and J. Xu, Synthesis, structure and characterization of $M(IO_3)_2(HIO_3)$ (M = Ca, Sr) as new anhydrous alkaline earth metal bis-iodate hydrogeniodate compounds, Dalton Trans. **48**, 13074 (2019).

[70] G. X. He, Y. G. Chen, N. Yang, M. L. Xing, and X. M. Zhang, $KSbI_6O_{18}$: An antimony iodate semiconductor material with cyclic chiral S_6-symmetric hexaiodate, Inorg. Chem. Commun. **65**, 13 (2016).

[71] J. H. Zhang, Q. Wu, and W. Z. Lai, A study of composition effects on the bandgaps in a series of new alkali metal aluminum/gallium iodates, Dalton Trans. **49**, 2337 (2020).

[72] F. F. Mao, J. Y. Hu, B. X. Li, and H. Wu, $Bi_4O(I_3O_{10})(IO_3)_3(SeO_4)$: Trimeric condensation of IO_4^{3-} monomers into the $I_3O_{10}^{5-}$ polymeric anion observed in a three-component mixed-anion NLO material, Dalton Trans. **49**, 15597 (2020).

[73] C. K. Aslani, V. V. Klepov, M. A. A. Aslani, and H. C. Zur Loye, Hydrothermal synthesis of new iodates $Ln_2(IO_3)_3(IO_4)$ (Ln = La, Nd, Pr) containing the tetraoxoiodate(V) Anion: creation of luminescence properties by doping with Eu, Dy, and Tb, Cryst. Growth Des. **21**, 4707 (2021).

[74] Y. Li, J. Huang, and H. Chen, Crystal growth, characterization and theoretical studies of the noncentrosymmetric compound $Al_3(IO_3)_9 \cdot (HIO_3)_6 \cdot 18H_2O$, J. Alloys Compd. **856**, 157852 (2021).

[75] G. Peng, C. Lin, H. Fan, K. Chen, B. Li, G. Zhang, and N. Ye, $Be_2(BO_3)(IO_3)$: The first anion-mixed van der Waals member in the KBe_2BO_3F family with a very strong second harmonic generation response, Angew. Chemie - Int. Ed. **60**, 17415 (2021).

[76] M. Ding, H. Yu, Z. Hu, J. Wang, and Y. Wu, $Na_7(IO_3)(SO_4)_3$: The First noncentrosymmetric alkaline-metal iodate-sulfate with isolated $[IO_3]$ and $[SO_4]$ units, Chem. Commun. **57**, 9598 (2021).

[77] T. Y. Chang, B. P. Yang, C. L. Hu, D. Yan, and J. G. Mao, $M(IO_3)(HPO_4)(H_2O)$ (M = Sc, Fe, Ga, In): Introduction of Phosphate Anions into Metal Iodates, Cryst. Growth Des. **17**, 4984 (2017).

[78] H. Song, N. Wang, Y. Li, W. Liu, Z. Lin, J. Yao, and G. Zhang, SrI_3O_9H: A new alkaline earth metal iodate with two different anionic units using mild aqua-solution method, Solid State Sci. **97**, 105982 (2019).

[79] Y. Xu, C. Lin, D. Zhao, B. Li, L. Cao, N. Ye, and M. Luo, Chemical substitution-oriented design of a new polar $PbFIO_3$ achieving a balance between large second-harmonic generation response and wide band gap, Scr. Mater. **208**, 114347 (2022).

[80] D. Wang, X. Jiang, P. Gong, X. Zhang, Z. Lin, Z. Hu, and Y. Wu, A new $I_3O_9^{3-}$ group constructed from IO_3^- and IO_5^{5-} anion units in $Cs_3[Ga_2O(I_3O_9)(IO_3)_4(HIO_3)]$, CrystEngComm **24**, 77 (2022).

[81] M. Gai, T. Tong, Y. Wang, Z. Yang, and S. Pan, New alkaline-earth metal fluoroiodates exhibiting large birefringence and short ultraviolet cutoff edge with highly polarizable $(IO_3F)^{2-}$ units, Chem. Mater. **32**, 5723 (2020).

[82] Y. H. Kim, T. T. Tran, P. S. Halasyamani, and K. M. Ok, Macroscopic polarity control with alkali metal cation size and coordination environment in a series of tin iodates, Inorg. Chem. Front. **2**, 361 (2015).